Energy-Optimal Control for Autonomous Underwater Vehicles Using Economic Model Predictive Control

Niankai Yang, *Graduate Student Member, IEEE*, Dongsik Chang, *Member, IEEE*, Matthew Johnson-Roberson, and Jing Sun, *Fellow, IEEE*

***Abstract*— Improving endurance is important for autonomous underwater vehicles (AUVs) as it affects the operational cost and application range of the vehicle. In this article, we propose an economic model predictive control (EMPC)-based controller to reduce the control energy of AUVs while performing waypoint tracking. The proposed EMPC controller optimizes stage costs capturing the control energy consumed within the prediction horizon and a terminal cost approximating the energy-to-go, the energy required to reach the desired waypoint from the end of the prediction horizon. To approximate the energy-to-go, we partition it into the dynamic and static segments based on the operational characteristics of the optimal vehicle maneuver obtained from off-line trajectory optimization using direct collocation (DC). To account for the disturbances caused by ocean currents, we adopt the energy-to-go to a virtual Earth-fixed frame that transforms the drift in the vehicle location to the drift in the desired waypoint. Theoretical and numerical analyses of the approximated energy-to-go reveal that the proposed controller can balance the tradeoffs among energy components spent for vehicle surge, heave, and yaw controls in consideration of vehicle dynamics. Simulations under different flow conditions are conducted to compare the proposed approach with DC and a line-of-sight (LOS) guidance-based approach that optimizes vehicle surge speed for energy minimization. Through simulations, it is shown that the proposed approach achieves near-optimal performance as DC and outperforms the LOS-based approach.**

***Index Terms*— Autonomous underwater vehicle (AUV), control-oriented AUV model, economic model predictive control (EMPC), energy management, energy-efficient maneuver, energy-optimal control, waypoint tracking.**

Manuscript received October 8, 2021; accepted January 5, 2022. Recommended by Associate Editor E. Zergeroglu. *(Corresponding author: Niankai Yang.)*

Niankai Yang and Jing Sun are with the Department of Naval Architecture and Marine Engineering, University of Michigan, Ann Arbor, MI 48109 USA (e-mail: ynk@umich.edu; jingsun@umich.edu).

Dongsik Chang was with the Department of Naval Architecture and Marine Engineering, University of Michigan, Ann Arbor, MI 48109 USA. He is now with the Collaborative Robotics and Intelligent Systems Institute, Oregon State University, Corvallis, OR 97331 USA (e-mail: changdo@oregonstate.edu).

Matthew Johnson-Roberson was with the Department of Naval Architecture and Marine Engineering, University of Michigan, Ann Arbor, MI 48109 USA. He is now with the Robotics Institute, School of Computer Science, Carnegie Mellon University, Pittsburgh, PA 15213 USA (e-mail: mkj@andrew.cmu.edu).

Color versions of one or more figures in this article are available at https://doi.org/10.1109/TCST.2022.3143366.

Digital Object Identifier 10.1109/TCST.2022.3143366

NOMENCLATURE

α	Coefficient in the thruster power model.
β	Control parameter affecting the sharpness of the turn.
$\Delta\psi$	Difference between the desired and present course directions of the vehicle [rad].
Γ_d	Travel time in the dynamic part of the energy-to-go [s].
Γ_s	Travel time in the static part of the energy-to-go [s].
ϕ, θ, ψ	Roll, pitch, and yaw angle in the Earth-fixed frame [rad].
ψ_d	Variation in the course direction of the vehicle during the dynamic mode [rad].
B, W	Vehicle buoyancy and weight [N].
$h_p(\cdot)$	Relationship between thrust and power consumption.
I_{zz}	Moment of inertia around the heave direction [$\text{kg} \cdot \text{m}^2$].
$K_{\dot{p}}, M_{\dot{q}}, N_{\dot{r}}$	Roll, pitch, and yaw added mass [$\text{kg} \cdot \text{m}^2/\text{rad}$].
K_p, M_q, N_r	Roll, pitch, and yaw damping coefficient [$\text{kg} \cdot \text{m}^2/(\text{s} \cdot \text{rad})$].
l_i	Distance between vertical thrusters and the midship ($i = 1$), distance between horizontal thrusters and the center line of the vehicle ($i = 2$), and vertical distance between horizontal thrusters and the vehicle center of gravity ($i = 3$) [m].
m	Vehicle total mass [kg].
p, q, r	Roll, pitch, and yaw rate in the body-fixed frame [rad/s].
P^i	Power for nullifying positive buoyancy ($i =$ PB) and overcoming surge drag force ($i =$ SD) [W].
T^i	Left ($i = 1$), right ($i = 2$), back ($i = 3$), and front ($i = 4$) thruster inputs [N].
u, v, w	Surge, sway, and heave velocity in the body-fixed frame [m/s].
u_c, v_c, w_c	Ocean current velocity along the surge, sway, and heave direction [m/s].

u_r, v_r, w_r	Relative surge, sway, and heave velocity with reference to the currents in the body-fixed frame [m/s].
V_c^i	Ocean current velocity along the x, y, and z direction ($i = x, y, z$) [m/s].
x, y, z	x, y, and z position in the Earth-fixed frame [m].
$X_{\dot{u}}, Y_{\dot{v}}, Z_{\dot{w}}$	Surge, sway, and heave added mass [kg].
X_u, Y_v, Z_w	Surge, sway, and heave damping coefficient [kg/s].

I. Introduction

AUTONOMOUS underwater vehicles (AUVs) have advanced and accelerated underwater explorations due to their ability to operate in hazardous and unstructured environments [1]. Yet, more than 80% of the underwater areas on the Earth remain unexplored [2]. One of the major reasons for this low exploration rate is the limited vehicle endurance, which restricts the travel range and increases the operational costs of AUVs. For improved endurance, a wide variety of AUVs has been developed, e.g., buoyancy-driven vehicles and hybrid vehicles with both buoyancy- and propeller-driven propulsion mechanisms. Although buoyancy-driven vehicles (e.g., underwater gliders) have become central to oceanographic missions [3], their low maneuverability (e.g., restricted steering and acceleration) limits their application for tasks, such as benthic survey and mapping [4]. Extending the endurance of propeller-driven AUVs for underwater survey and mapping research remains an active and important research topic, which will be the focus of this article.

A common approach for improving AUV endurance is to plan energy-optimal references (e.g., waypoints, paths, or trajectories) in consideration of ocean currents [5]–[7]. By leveraging the favorable currents while avoiding the adverse ones [8], the optimized vehicle references reduce the vehicle operational energy, thereby increasing vehicle endurance. However, due to the intensive computation of planning algorithms [9], reference planning is typically performed based on simplified vehicle models (e.g., kinematic model) and predicted ocean conditions. Consequently, a reference-following controller is required to account for the uncertainties in the vehicle model and ocean currents, and the vehicle energy efficiency achieved by following the planned reference relies critically on the energy-saving performance of the reference-following controller.

To reduce the energy consumed by following the planned reference, various optimal control approaches were adopted. For example, the cost function of the model predictive control (MPC) in [10] and [11] was formulated as a combination of reference-following error and control efforts to save energy during AUV horizontal maneuvers. In [12], a linear quadratic regulator was developed using a cost containing a control effort term to balance the AUV depth tracking performance and energy consumption. Reinforcement learning-based strategies were proposed in [13]–[15] to achieve energy-efficient maneuvers for unmanned surface and aerial vehicles. These controllers can reduce vehicle energy use by generating thrusts that minimize the weighted sum of reference-following error and control efforts. Nevertheless, constant weighting cannot accommodate the tradeoff in reference-following performance and energy consumption under different operational conditions. Consequently, the energy-saving potential of these controllers is not fully explored.

In this article, considering waypoints as the planned references, we design an energy-optimal controller for a waypoint tracking problem. We propose an energy-optimal AUV control design based on economic model predictive control (EMPC) that explicitly incorporates the vehicle dynamics, ocean currents, and reference-following performance into the energy minimization. In particular, we formulate the terminal cost of EMPC in terms of the energy required to reach the destination beyond the prediction horizon, referred to as energy-to-go. By analyzing the energy-optimal solution obtained from off-line trajectory optimization using direct collocation (DC), we partition the energy-to-go into the dynamic and static parts and parameterize each part with its duration. The effects of ocean currents on the energy-to-go are further incorporated by accounting for the drift in vehicle locations due to the ocean currents. The proposed approach is first compared with the optimal solution from DC to show its near-optimal performance. Then, an extensive comparison is conducted between the proposed approach and a line-of-sight (LOS) guidance-based control approach that optimizes vehicle surge speed for energy minimization based on vehicle kinematics. Simulation results under various current conditions demonstrate that the proposed approach could substantially improve energy efficiency.

This article extends our conference articles [16], [17] with its main contributions given as follows.

1) It presents an energy-optimal control framework that can optimize vehicle energy by explicitly considering vehicle dynamics and ocean currents.
2) It provides an approach to formulate the terminal cost in EMPC for enhanced energy efficiency by leveraging off-line trajectory optimization solutions.
3) It analyzes the approximated energy-to-go to reveal the tradeoffs among energy components spent for controlling the vehicle motions in different degrees of freedom (DOFs) and provides insights for controller design.

The remainder of this article is organized as follows. Section II introduces the vehicle models and formulates the energy-optimal control problem of AUVs under currents. In Section III, DC is applied to address the energy-optimal control problem. In Section IV, the EMPC design is proposed with the analysis of its cost function. Section V verifies the proposed approach with simulation results obtained using different current conditions. Finally, conclusions and future work are given in Section VI.

II. Background

In this section, we first provide the details of our test-bed AUV to facilitate the subsequent modeling of the control authorities and vehicle power consumption. Based on the specifications of the test-bed AUV, we then introduce a six-DOF

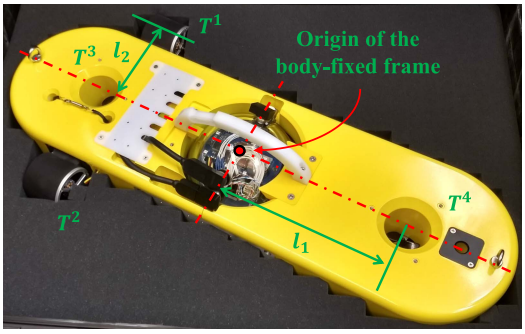

Fig. 1. Schematic of DROP-Sphere.

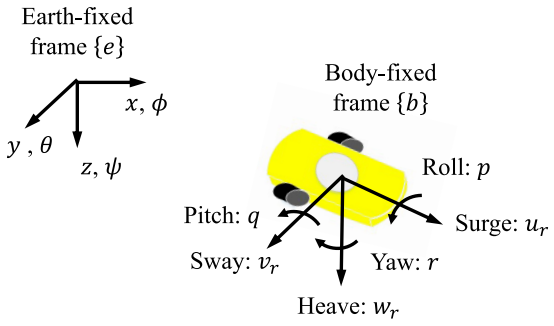

Fig. 2. Reference frames and notations.

motion model and an experimentally validated power consumption model. Finally, the energy-optimal control problem of AUVs under ocean currents is formulated.

A. DROP-Sphere Platform

A propeller-driven AUV, DROP-Sphere, developed by the DROP Lab at the University of Michigan for underwater benthic optical mapping [18], is adopted for the study in this article. The vehicle is an open-source and low-cost platform with an elliptical body of 0.86-m length, 0.43-m width, and 0.25-m height (as shown in Fig. 1). In the middle of the vehicle, a 0.2-m-diameter borosilicate glass sphere is used to house electronic equipment, such as the inertial measurement unit, an embedded computer, batteries, and cameras. For vehicle propulsion, four identical flooded brushless bidirectional motors with a maximum thrust of 7.86 N each are utilized. Two horizontal thrusters (T^1, T^2) control the surge and yaw motion of the vehicle, and two vertical ones (T^3, T^4) control its heave and pitch motion. DROP-Sphere has positive buoyancy, i.e., the vehicle's buoyancy ($B = 201.586$ N) exceeds its weight ($W = 200.116$ N), which guarantees the recovery of the vehicle in the case of thruster or battery failures [19].

B. Vehicle Motion Model

To capture the vehicle motion under ocean currents, two reference frames are used, as shown in Fig. 2. The velocities ($\boldsymbol{\nu} = [u, v, w, p, q, r]^T \in \mathbb{R}^6$) and control inputs ($\boldsymbol{\tau} \in \mathbb{R}^6$) are represented in a body-fixed frame. The positions and orientations ($\boldsymbol{\eta} = [x, y, z, \phi, \theta, \psi]^T \in \mathbb{R}^6$) are given in an Earth-fixed frame. Assuming that the ocean current is constant and irrotational, the velocity of ocean currents expressed in the Earth-fixed frame is denoted as $\mathbf{V}_c = [V_c^x, V_c^y, V_c^z, 0, 0, 0] \in \mathbb{R}^6$. The velocity of ocean currents in the body-fixed frame is denoted as $\boldsymbol{\nu}_c = [u_c, v_c, w_c, 0, 0, 0]^T \in \mathbb{R}^6$, which satisfies $\boldsymbol{V}_c = \mathbf{J}(\boldsymbol{\eta})\boldsymbol{\nu}_c$ with the coordinate transformation matrix $\mathbf{J}(\boldsymbol{\eta}) \in \mathbb{R}^{6\times6}$. Then, with reference to the current, the relative velocity of the vehicle in the body-fixed frame is computed as $\boldsymbol{\nu}_r = \boldsymbol{\nu} - \boldsymbol{\nu}_c = [u_r, v_r, w_r, p, q, r]^T \in \mathbb{R}^6$.

Based on the defined notations, the vehicle kinematic and dynamic relationships (see [20], [21]) are given as

$$\dot{\boldsymbol{\eta}} = \mathbf{J}(\boldsymbol{\eta})\boldsymbol{\nu}_r + \mathbf{V}_c \tag{1a}$$

$$\mathbf{m}_t\dot{\boldsymbol{\nu}}_r + \mathbf{f}_c(\boldsymbol{\nu}_r) + \mathbf{f}_h\boldsymbol{\nu}_r + \mathbf{f}_g(\boldsymbol{\eta}) = \boldsymbol{\tau} \tag{1b}$$

where $\mathbf{m}_t = \mathbf{m}_{rb} + \mathbf{m}_a$ is the vehicle total mass matrix with matrices of the rigid body mass $\mathbf{m}_{rb} \in \mathbb{R}^{6\times6}$ and the added mass $\mathbf{m}_a \in \mathbb{R}^{6\times6}$. $\mathbf{f}_c(\boldsymbol{\nu}_r) \in \mathbb{R}^6, \mathbf{f}_h \in \mathbb{R}^{6\times6}$, and $\mathbf{f}_g(\boldsymbol{\eta}) \in \mathbb{R}^6$ represent the Coriolis and centripetal force, the hydrodynamic damping force, and hydrostatic force matrices, respectively. The added mass and hydrodynamic damping matrices are considered as

$$\mathbf{m}_a = \operatorname{diag}\left(X_{\dot{u}}, Y_{\dot{v}}, Z_{\dot{w}}, K_{\dot{p}}, M_{\dot{q}}, N_{\dot{r}}\right) \tag{2a}$$

$$\mathbf{f}_h = \operatorname{diag}\left(X_u, Y_v, Z_w, K_p, M_q, N_r\right) \tag{2b}$$

where diag$(\cdot)$ denotes a diagonal matrix. $X_{\dot{u}}$, $Y_{\dot{v}}$, $Z_{\dot{w}}$, $K_{\dot{p}}$, $M_{\dot{q}}$, and $N_{\dot{r}}$ are the added mass coefficients, and X_u, Y_v, Z_w, K_p, M_q, and N_r are the hydrodynamic damping coefficients. The assumption that the hydrodynamic damping forces and moments are linear with respect to vehicle relative velocities generally only holds when the vehicle relative velocities are low, as in energy-efficient maneuvers when the speed is typically less than 0.5 m/s to avoid large power consumption [16], [22].

The control input vector $\boldsymbol{\tau}$ relates to the DROP-Sphere thrusts as

$$\boldsymbol{\tau} = \begin{bmatrix} T^1 + T^2 \\ 0 \\ T^3 + T^4 \\ 0 \\ (T^1 + T^2)l_3 + (T^3 - T^4)l_1 \\ (T^1 - T^2)l_2 \end{bmatrix}^T \tag{3}$$

where l_1 is the distance between vertical thrusters and the midship, l_2 is the distance between horizontal thrusters and the center line, and l_3 is the vertical distance between horizontal thrusters and the center of gravity. The pitch moment $(T^1 + T^2)l_3$ is induced by the misalignment between the horizontal thrusters and the depth of the vehicle gravity center. For all the numerical values of the coefficients in the models, see Appendix I.

C. Thruster Power Consumption Model

In this work, the thruster propulsion energy is the major energy consumption for vehicle operation. The following empirical model captures the power consumed by each thruster

$$h_p\left(T^i\right) = \alpha\left(T^i\right)^2, \quad \text{for } i = 1, 2, 3, 4 \tag{4}$$

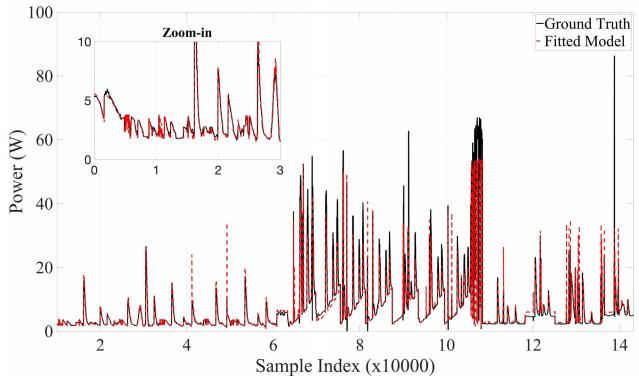

Fig. 3. Validation of the thruster power consumption model.

and the energy consumption is calculated by integrating (4). The power conversion ratio $\alpha = 0.4364$ is derived from the DROP-Sphere experimental data collected at the towing tank located at the University of Michigan. During the experiment, two horizontal thrusters were commanded to drive the vehicle for consecutive straight-line and turning maneuvers in the horizontal plane. The thrusts and the power consumption of two horizontal thrusters are measured. The comparison between the power consumption from the experimental data and that from the model in (4) is provided in Fig. 3. The mean absolute error between the true and predicted power is 1.4 W. As seen in the zoomed-in plot of Fig. 3, the empirical model can well capture the thruster power consumption except in extremely high-power regions.

D. Energy-Optimal Control Problem

Consider an underwater exploration mission for an AUV with a sequence of N_w waypoints, $\mathcal{WP} = \{\text{WP}_i \in \mathbb{R}^2,\ i = 0, \ldots, N_w\}$, given by the planning algorithm, where $\text{WP}_i = (\text{WP}_i^x, \text{WP}_i^y)$ contains the x and y locations of the ith waypoint, and WP_0 corresponds to the initial location of the vehicle. All the waypoints are assumed to be at the same depth as the vehicle initial depth, and the vehicle is initialized with zero relative velocities and a heading toward WP_1. The energy-optimal control problem is formulated as

$$\min_{\{T_k^1\},\{T_k^2\},\{T_k^3\},\{T_k^4\}} J = \sum_{k=0}^{N_f-1}\sum_{i=1}^{4} h_p\left(T_k^i\right)\Delta t \tag{5a}$$

$$\text{s.t.}\quad \boldsymbol{\chi}_{k+1} = \mathbf{f}_{dt}(\boldsymbol{\chi}_k, T_k^i, \mathbf{V}_{c,k}), \quad \boldsymbol{\chi}_0 = \boldsymbol{\chi}_{init} \tag{5b}$$

$$|T_k^i| \le \bar{T}, \quad |\Delta z_k| = |z_k - z_0| \le \bar{z} \tag{5c}$$

$$|\phi_k| \le \bar{\phi}, \quad |\theta_k| \le \bar{\theta} \tag{5d}$$

$$\forall \text{WP}_j \in \mathcal{WP},\ \exists \boldsymbol{\chi}_{m_j},\ \text{where } m_j \in [0, N_f] \text{ and } m_0 \le m_1 \le \cdots \le m_{N_w},\ \text{such that}$$

$$\sqrt{\left(x_{m_j} - \text{WP}_j^x\right)^2 + \left(y_{m_j} - \text{WP}_j^y\right)^2} \le r_{\text{COA}} \tag{5e}$$

where $\boldsymbol{\chi} = [\boldsymbol{\nu}_r, \boldsymbol{\eta}]$ is the states of the vehicle, $\mathbf{f}_{dt}(\cdot)$ is the discrete-time vehicle kinematics and dynamics obtained by discretizing (1) with time step Δt, $\{T_k^i\}$ denotes the input sequence of the i^{th} thruster, N_f is the total number of time steps, $\bar{T}$ is the thruster limit, $\boldsymbol{\chi}_{\text{init}}$ is the initial condition of the vehicle, and r_{COA} is the radius of the circle of acceptance (COA). $\bar{z}$, $\bar{\phi}$, and $\bar{\theta}$ are the upper bounds of the deviation in depth, roll angle, and pitch angle, respectively, The constraint (5e) is included to ensure that the vehicle will sequentially visit all the waypoints by entering the COA of each waypoint.

For simplicity, we make the following assumptions about the environment: 1) the vertical velocity component of ocean currents is negligible compared to the motion of the vehicle [23]; 2) the environment is obstacle-free; and 3) the magnitude of ocean currents is less than the maximum surge speed of the vehicle to guarantee complete reachability. In the case of strong currents or the presence of obstacles, the waypoints can be replanned to ensure the satisfaction of assumptions 2) and 3). In addition, we assume that the knowledge of the vehicle states and the ocean flow velocity at the vehicle location contains negligible errors, which can be achieved with advanced sensor fusion algorithms and appropriate sensors [24], [25].

III. Globally Optimized Vehicle Maneuver Simulation and Analysis

In this section, we first solve the energy-optimal control problem formulated in Section II-D using off-line trajectory optimization. The solution will provide a benchmark for evaluating the performance of the proposed approach. Then, we analyze the characteristics of the optimal maneuver to facilitate the subsequent controller development.

A. Trajectory Optimization Using Direct Collocation

To solve the energy-optimal control problem in Section II-D, we apply DC [26] for trajectory optimization, which employs the following steps to compute the optimal vehicle thrust sequences. First, the vehicle input and state trajectories from the initial condition to the desired end condition are equally discretized with a constant time step size. Based on the discretization, the trajectory optimization problem is reformulated as a nonlinear programming (NLP) problem using the discretized states and inputs as the decision variables. For the NLP, the objective function is the sum of propulsion energy evaluated using the discretized inputs, and the constraint is that two adjacent states and the corresponding inputs should satisfy the vehicle dynamics. Finally, the NLP is solved numerically to obtain the optimal vehicle thrust sequences.

To examine the energy-optimal vehicle motion and behavior using DC, we consider a case study where an AUV is required to sequentially visit two waypoints, as shown in Fig. 4(a). The parameters for the constraints are chosen as $\bar{T} = 7.86$ N, $\bar{z} = 0.005$ m, $\bar{\phi} = 0.7$ rad, $\bar{\theta} = 0.02$ rad, and $r_{\text{COA}} = 2$ m. Considering that the ocean currents are modeled as disturbances in vehicle kinematics, and they will not change the nature of vehicle dynamics, especially in terms of the relative velocity, we study the case where the velocity of ocean currents is zero to facilitate the analysis of the dynamic characteristics of the energy-efficient maneuvers. The insights from this case study can be extended to arbitrary ocean current velocities, as to be discussed in Section IV.

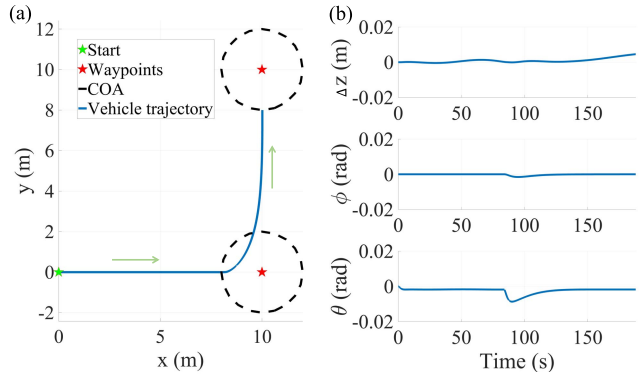

Fig. 4. Vehicle trajectories from the DC (green arrows in (a) indicate the sequence of the waypoints; Δz denotes the deviation from the desired depth).

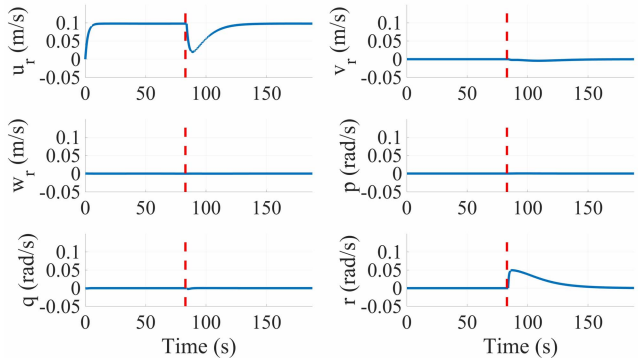

Fig. 5. Vehicle relative velocities of the DC solution (red dashed line indicates the instance when the vehicle switches its destination to the second waypoint).

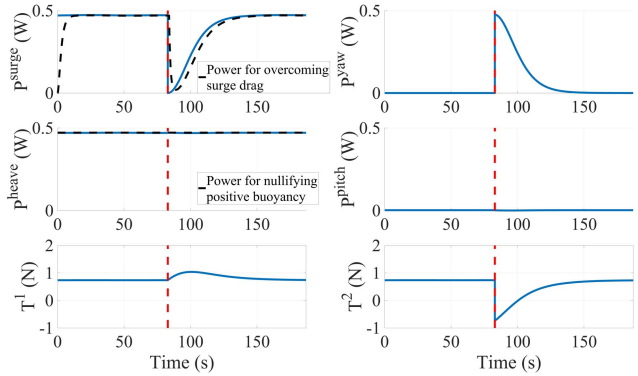

Fig. 6. Vehicle power consumption and thrusts of the DC solution (red dashed line indicates the instance when the vehicle switches its destination to the second waypoint; the power for overcoming surge drag and the power for nullifying positive buoyancy are derived with $2h_p(X_u u_r/2)$ and $2h_p((B-W)/2)$, respectively).

In this case study, a waypoint tracking problem is decomposed and solved as multiple waypoint tracking problems between two sequential waypoints. For each waypoint tracking problem, we first compute the optimal vehicle trajectories from the current vehicle location to the desired waypoint using DC. Then, the DC solution is executed until the vehicle reaches the COA of the desired waypoint. By considering only two waypoints at a time, the solution may have deteriorated energy efficiency compared to the global optimal solution that considers all waypoints at the same time. However, it makes the problem computationally more tractable, especially for long missions. Moreover, this approach is less likely to suffer from robustness issues (e.g., missing the waypoint) or performance degradation under model uncertainties and waypoint replanning [27]. With discretization of the trajectories for each waypoint tracking problem into 100 segments, the optimal solution from the DC is given in Fig. 4, which shows that the DC can drive the vehicle to sequentially visit the waypoints while maintaining its depth, roll angle, and pitch angle. However, the computation for solving each NLP in the above case study is intensive (e.g., about 200 s for each segment on a 2.9-GHz Intel Core i5 processor with 16-GB RAM), making it prohibitive as a real-time energy-optimal control strategy for resource-limited AUV platforms.

B. Analysis of the Optimal Maneuver

Since the DC solution represents a globally optimized maneuver for each waypoint tracking problem, we analyze the characteristics of the optimal maneuver to guide the subsequent controller development. The vehicle relative velocities of the DC solution are given in Fig. 5, and the vehicle power consumption and horizontal thruster inputs are given in Fig. 6. According to Figs. 5 and 6, we make the following remarks on the desired energy-optimal maneuvering:

Remark 1 (Pitch and Heave Control): The pitch power and relative heave velocity are nearly zero over the entire operation, indicating that the pitch control energy and the heave motion are negligible. The constant heave power is mainly used for overcoming the vehicle's positive buoyancy. Thus, the energy-saving potential for optimizing heave and pitch control is minimal.

Remark 2 (Surge Control): The surge power is mainly used for overcoming the surge drag force over the entire operation except when the vehicle performs the initial acceleration.

Remark 3 (Static and Dynamic Modes): Two distinctive modes can be identified, which we refer to as static mode and dynamic mode. In the static mode, the vehicle has a constant surge speed with minimal motion in other DOFs, and yaw and pitch power consumptions are negligible. In the dynamic mode, the vehicle has a nonzero yaw rate, and energy is used for surge, heave, and yaw controls. The dynamic mode happens only when the vehicle needs to change its direction (e.g., waypoint switch). Typically, the vehicle first turns to its desired heading then keeps its course (i.e., first dynamic mode and then static mode). The characteristics of the two modes can also be observed from the variations in the difference between horizontal thrusts over the entire operation.

IV. Energy-Optimal EMPC for AUV Energy-Optimal Control

In this section, we propose an online control design that addresses the energy-optimal control problem formulated in Section II-D. Based on the analysis in Section III-B, we first propose a decoupled controller design with an EMPC to control the vehicle horizontal thrusters. Then, the terminal cost of

the EMPC is derived. Finally, we present the overall schematic of the energy-optimal EMPC and provide an analysis of the EMPC to show the tradeoffs in vehicle control energy.

A. Control Decoupling

Since the energy-saving potential of heave and pitch controls is minimum for horizontal vehicle maneuvers (see Remark 1), the heave and pitch controls from the vertical thrusters are decoupled from the energy-optimal control problem and achieved with two individual PID controllers to reduce the computation complexity. For the control of horizontal thrusters, we adopt the EMPC for the following reasons [28]. First, EMPC can explicitly minimize vehicle control energy with consideration of vehicle dynamics and thruster limits, assuring the feasibility of the control. Second, it can account for the long-term effect of control inputs on vehicle energy with the terminal cost.

Following the standard EMPC formulation, we optimize the horizontal thruster sequences $\{T^1_{k|t}\}$ and $\{T^2_{k|t}\}$ within the prediction horizon by minimizing the cost given as

$$J = \sum_{k=0}^{H-1} L_{k|t} + E \tag{6}$$

where $(\cdot)_{k|t}$ is the k-step ahead prediction made at time instant t, H is the prediction horizon, and E is the terminal cost. The stage cost $L_{k|t}$ is formulated as

$$L_{k|t} = \left(\sum_{i=1}^{2} h_p\left(T^i_{k|t}\right) + P^{\mathrm{PB}}\right)\delta t_L \tag{7}$$

where δt_L is the time step size within the prediction horizon, and the heave and pitch control power P^{PB} are approximated as

$$P^{\mathrm{PB}} = 2h_p((B-W)/2). \tag{8}$$

The optimization in (6) is performed subject to: 1) horizontal thrust limits ($\bar{T}$) and 2) control-oriented model derived from (1) based on the vehicle geometry and the energy-optimal maneuver observed in Section III-B (i.e., by assuming $w_r = p = q = \phi = \theta = 0$)

$$(m - X_{\dot{u}})\dot{u}_r = v_r \mathrm{rm} - X_u u_r + T^1 + T^2 \tag{9a}$$
$$(m - Y_{\dot{v}})\dot{v}_r = -u_r \mathrm{rm} - Y_v v_r \tag{9b}$$
$$(I_{zz} - N_{\dot{r}})\dot{r} = -N_r r + \left(T^1 - T^2\right) l_2 \tag{9c}$$
$$\dot{x} = \cos\psi u_r - \sin\psi v_r + V_c^x \tag{9d}$$
$$\dot{y} = \sin\psi u_r + \cos\psi v_r + V_c^y \tag{9e}$$
$$\dot{\psi} = r \tag{9f}$$

where (9a)–(9c) are the surge, sway, and yaw dynamics, (9d)–(9f) are the x, y, and yaw kinematics, m is the vehicle total mass, and I_{zz} is the moment of inertia around the heave direction.

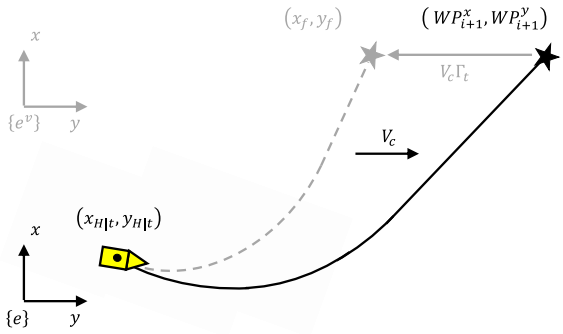

Fig. 7. Illustration of the virtual Earth-fixed frame to account for the drift effect of ocean currents V_c represented by the black arrow (the solid black line is the vehicle trajectory beyond the prediction horizon in the Earth-fixed frame; the dashed gray line is the vehicle trajectory beyond the prediction horizon in the virtual Earth-fixed frame; and the gray arrow indicates the drift in the desired waypoint).

B. EMPC Terminal Cost Formulation

To retain energy efficiency close to that from the DC solution, we design the terminal cost E in (6) to capture the energy-to-go, the energy required to reach the destination (i.e., the desired waypoint) beyond the prediction horizon. For computationally efficient numerical optimization, we derive an analytical expression for the energy-to-go through the following steps.

1) Accommodation of Ocean Currents: Motivated by [29], a virtual Earth-fixed frame $\{e^v\}$ is introduced to account for the effect of ocean currents on the vehicle motion (see Fig. 7). Define the virtual Earth-fixed frame as a frame that moves with the current such that the ocean current will be seen as zero in the virtual Earth-fixed frame. The vehicle motion in the virtual Earth-fixed frame and body-fixed frame under current can be captured with (1). Meanwhile, a fixed waypoint in the Earth-fixed frame will become a moving virtual destination in the virtual Earth-fixed frame, moving at the velocity equal to the opposite of the ocean current velocity. Finding the thrust profile that can drive the vehicle to the waypoint WP_{i+1} in the Earth-fixed frame in time Γ_t is then equivalent to finding the thrust profile that can drive the vehicle to the following virtual destination in the virtual Earth-fixed frame in time Γ_t:

$$\begin{cases} x_f = \mathrm{WP}^x_{i+1} - V_c^x \Gamma_t \\ y_f = \mathrm{WP}^y_{i+1} - V_c^y \Gamma_t. \end{cases} \tag{10}$$

Consequently, the problem of approximating the energy to reach WP_{i+1} under currents can be reformulated as approximating the energy to (x_f, y_f) under no current.

2) Energy-to-go Partition: To approximate the energy-to-go in the virtual Earth-fixed frame, recall the characteristics of the static and dynamic modes observed from the DC solution (see Remark 3). We then partition the energy-to-go into the dynamic and static parts and express the terminal cost as

$$E = E_d + E_s \tag{11}$$

where E_d and E_s approximate the dynamic and static parts in the energy-to-go, respectively. See Fig. 8 for an illustration of the two components in energy-to-go. To derive the dynamic

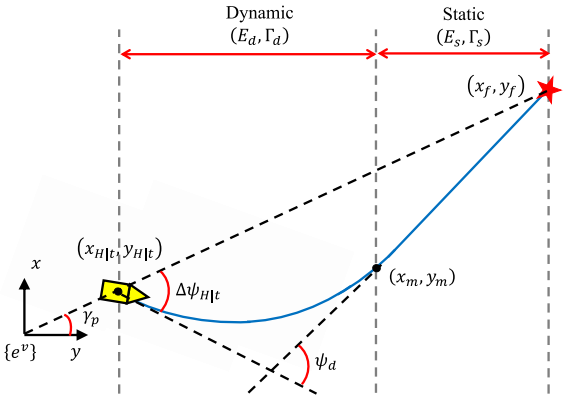

Fig. 8. Illustration of the dynamic and static parts (blue line indicates the vehicle trajectory beyond the prediction horizon).

and static parts, given that the vehicle control energy is closely related to its travel time, the travel time in the dynamic and static parts, denoted by Γ_d and Γ_s, respectively, are introduced as extra decision variables in EMPC, where $\Gamma_t = \Gamma_d + \Gamma_s$. Meanwhile, constraints on these decision variables are included in the optimization to ensure that a meaningful solution can be derived.

3) Energy Approximation in the Static Mode: In the static mode, the thruster power is mainly used for surge and heave controls, and the surge speed is nearly constant. Thus, we approximate the total power as

$$P_s = P^{\mathrm{PB}} + P^{\mathrm{SD}} \tag{12}$$

where $P^{\mathrm{SD}} = 2h_p(X_u u_{r,H|t}/2)$ is the power for overcoming the surge drag force under constant surge speed. Then, the static part of the energy-to-go is approximated with

$$E_s = P_s \Gamma_s. \tag{13}$$

To ensure that the vehicle can move from the location at the end of the dynamic mode (x_m, y_m) to the destination in Γ_s with constant surge speed and heading, we need a constraint on Γ_s. Considering that the vehicle trajectory is nearly a straight line, an equality constraint is imposed as

$$\Gamma_s = \frac{\sqrt{(y_f - y_m)^2 + (x_f - x_m)^2}}{U_v} \tag{14}$$

where $U_v = u_{r,H|t}$ approximates the vehicle total speed in the virtual Earth-fixed frame.

4) Energy Approximation in the Dynamic Mode: In the dynamic mode, the thruster energy is consumed for surge, heave, and yaw controls. The heave power is for nullifying the positive buoyancy and, thus, can be approximated with P^{PB}. The thrusts required for the surge and yaw controls can be derived from (9a) and (9c) given by

$$\begin{cases} T^1_{k|t} = \dfrac{X_u u_{r,k|t}}{2} + \dfrac{(I_{zz} - N_{\dot r})\dot r_{k|t} + N_r r_{k|t}}{2l_2} \\ T^2_{k|t} = \dfrac{X_u u_{r,k|t}}{2} - \dfrac{(I_{zz} - N_{\dot r})\dot r_{k|t} + N_r r_{k|t}}{2l_2} \end{cases} \tag{15}$$

for $k \geq H$. Note that the surge power is mainly consumed for overcoming the surge drag force in the dynamic mode

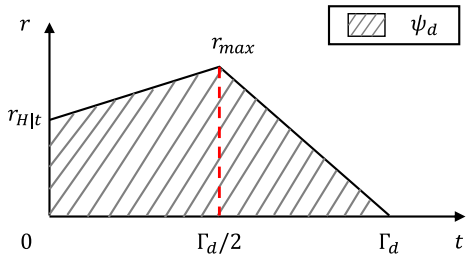

Fig. 9. Approximation of the yaw rate profile during the dynamic mode.

(see Remark 2). Thus, the thrusts for the surge control in the dynamic mode share the same parameterization as that in the static mode.

To obtain the thrusts from (15), we then assume $u_{r,k|t} = u_{r,H|t}$ for $k \geq H$. Namely, the thrusts for surge control are assumed to remain the same beyond the prediction horizon. Denote the variation in the course direction of the vehicle during the dynamic mode as ψ_d (see Fig. 8). To achieve the desired change in the heading, the yaw rate is assumed to increase to a maximum yaw rate ($r_{\max}$) in the first half of the dynamic mode and then decreases to zero in the rest of the dynamic mode, as shown in Fig. 9. Mathematically, the yaw rate is expressed as

$$r_{k|t} = \begin{cases} r_{H|t} + a_1(k-H)\delta t_d, & H \leq k \leq \dfrac{\Gamma_d}{2\delta t_d} + H \\ r_{\max} + a_2\left((k-H)\delta t_d - \dfrac{\Gamma_d}{2}\right), & \dfrac{\Gamma_d}{2\delta t_d} + H \leq k \leq \dfrac{\Gamma_d}{\delta t_d} + H \end{cases} \tag{16}$$

where $r_{\max} = 2\psi_d/\Gamma_d - 0.5 r_{H|t}$, $a_1 = 2(r_{\max} - r_{H|t})/\Gamma_d$ represents the $\dot r$ in the first half of the dynamic mode, $a_2 = -2r_{\max}/\Gamma_d$ represents the $\dot r$ in the second half of the dynamic mode, and δt_d is the time step size in the dynamic mode.

With (15) and (16), we can derive the surge and yaw power in the dynamic mode with arbitrary δt_d. To permit a computationally-efficient implementation, δt_d is chosen as half of the travel time in the dynamic mode, i.e., $\Gamma_d/2$. Then, following the trapezoid rule, the power in the dynamic mode is approximated using the power to generate the thrusts at the end of the prediction horizon ($T^i_{H|t}$), the middle of the dynamic mode ($T^i_{H+1|t}$), and the end of the dynamic mode ($T^i_{H+2|t}$) as

$$\begin{aligned} P_d &= P^{\mathrm{PB}} + \sum_{i=1}^{2} \frac{h_p\left(T^i_{H|t}\right) + 2h_p\left(T^i_{H+1|t}\right) + h_p\left(T^i_{H+2|t}\right)}{4} \\ &= P^{\mathrm{PB}} + P^{\mathrm{SD}} + P^{\mathrm{yaw}} \end{aligned} \tag{17}$$

where $h_p(T^i_{H+1|t})$ is the average of the power to generate the thrust at the middle of the dynamic mode when $\dot r = a_1$, and when $\dot r = a_2$, P^{yaw} is the power for yaw control given as

$$P^{\mathrm{yaw}} = c_0 + \frac{c_1}{\Gamma_d} + \frac{c_2}{\Gamma_d^2} + \frac{c_3}{\Gamma_d^3} + \frac{c_4}{\Gamma_d^4} \tag{18}$$

and c_i $(i = 0, \ldots, 4)$ are coefficients of the approximated yaw power. See Appendix II for the detailed derivation of (17) and

(18). Consequently, the dynamic part of the energy-to-go can be expressed by

$$E_d = P_d \Gamma_d. \tag{19}$$

To ensure that the vehicle can move from $(x_{H|t}, y_{H|t})$ to (x_m, y_m) in Γ_d with the approximated thrusts, we may need to evaluate the vehicle dynamics, which can be nontrivial. In this study, we make the following assumptions to derive the relationship between $(x_{H|t}, y_{H|t})$ and (x_m, y_m). First, ψ_d is assumed as $2\beta\Delta\psi_{H|t}$, where $\Delta\psi_{H|t} = \text{atan2}(y_f - y_{H|t}, x_f - x_{H|t}) - \tan^{-1}(v_{r,H|t}/u_{r,H|t}) - \psi_{H|t}$ is the difference between the desired and present course directions of the vehicle at the end of prediction horizon, and atan2(y,x) generalizes $\tan^{-1}$(y/x) to consider the signs of x and y and returns an angle between $-\pi$ to π. Second, (x_m, y_m) is assumed to be located on the line between $(x_{H|t}, y_{H|t})$ and (x_f, y_f). Then, (x_m, y_m) can be given based on vehicle kinematics (i.e., constant surge, sway, and yaw velocities) as

$$\begin{cases} x_m = x_{H|t} + \dfrac{U_v \Gamma_d \sin(\beta\Delta\psi_{H|t}) \cos(\gamma_p)}{\beta\Delta\psi_{H|t}} \\ y_m = y_{H|t} + \dfrac{U_v \Gamma_d \sin(\beta\Delta\psi_{H|t}) \sin(\gamma_p)}{\beta\Delta\psi_{H|t}} \end{cases} \tag{20}$$

where γ_p is the course direction between $(x_{H|t}, y_{H|t})$ and (x_f, y_f). Note that β will be a tuning parameter of the control that affects the sharpness of the turn, and an extensive discussion on the effect of β will be made in Section V-C.

C. Energy-Optimal EMPC Formulation and Analysis

By incorporating the approximated energy-to-go presented in Section IV-B, the proposed EMPC is given as

$$\min_{\{T^1_{k|t}\},\{T^2_{k|t}\},\Gamma_d,\Gamma_s} \quad J = \sum_{k=0}^{H-1} L_{k|t} + P_d\Gamma_d + P_s\Gamma_s \tag{21a}$$

$$\text{s.t.} \quad \boldsymbol{\zeta}_{k+1|t} = \mathbf{f}^h_{dt}(\boldsymbol{\zeta}_{k|t}, T^1_{k|t}, T^2_{k|t}, \mathbf{V}_{c,k|t}), \quad \boldsymbol{\zeta}_{0|t} = \boldsymbol{\zeta}_t \tag{21b}$$

$$|T^1_{k|t}| \le \bar{T}, \quad |T^2_{k|t}| \le \bar{T}, \quad 0 < u_{r,k+1|t} \tag{21c}$$

$$U_v\left(\frac{\Gamma_d \sin(\beta\Delta\psi_{H|t})}{\beta\Delta\psi_{H|t}} + \Gamma_s\right) = d \tag{21d}$$

where $\boldsymbol{\zeta} = [u_r, v_r, r, x, y, \psi]$ is the states of the vehicle in the horizontal plane, $\mathbf{f}^h_{dt}(\cdot)$ is the discrete-time vehicle kinematics and dynamics in the horizontal plane obtained by discretizing (9) with time step δt_L, and $d = ((y_f - y_{H|t})^2 + (x_f - x_{H|t})^2)^{1/2}$ is the required traveling distance in the virtual Earth-fixed frame. From (21), it can be seen that we parameterized the energy-to-go with Γ_s and Γ_d while enforcing a constraint (21d) on Γ_s and Γ_d to guarantee the satisfaction of vehicle motion model. The constraint (21d) is obtained from merging the kinematic constraints in (14) and (20).

The energy-optimal EMPC (EO-EMPC) is then proposed by combining the EMPC for controlling the horizontal thrusters and PIDs for controlling the vertical thrusters (see Fig. 10). By regrouping the terms in the approximated energy-to-go, the terminal cost is expressed as

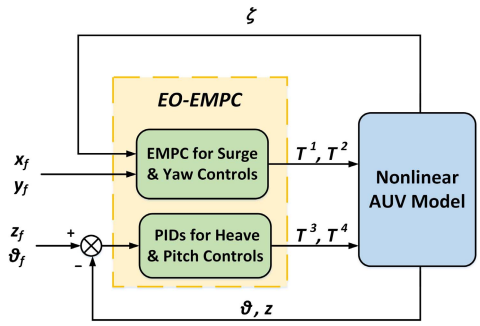

Fig. 10. Control architecture for the proposed EO-EMPC (z_f and θ_f are the desired depth and pitch angle, respectively).

$$\begin{aligned} E &= P_d\Gamma_d + P_s\Gamma_s \\ &= \underbrace{(P^{\text{PB}} + P^{\text{SD}})(\Gamma_d + \Gamma_s)}_{\text{Surge \& Heave Energy}} + \underbrace{P^{\text{yaw}}\Gamma_d}_{\text{Yaw Energy}}. \end{aligned} \tag{22}$$

From (22), we can see that two tradeoffs in vehicle control energy are captured by the approximated energy-to-go.

1) *Surge Versus Heave:* The tradeoff between the energy components for surge and heave controls appears in both dynamic and static modes. Since heave power P^{PB} is constant, a shorter travel time is desirable for reducing heave energy. However, considering that surge power is proportional to the squared surge speed, a shorter travel time will lead to larger energy spent for surge control.
2) *Surge Versus Heave Versus Yaw:* In the dynamic mode, the tradeoff between the energy components for surge and heave controls will also be affected by the energy component for yaw control. Since a lower turning rate requires smaller yaw moments, a slower turn (i.e., larger Γ_d) consumes less yaw power, as is demonstrated with (18). However, an overly slow turn will lead to an extremely long travel time. Since the energy is the time integral of power, the yaw energy can also be large for an overly slow turn (i.e., $c_0\Gamma_d$ dominates the yaw energy). Therefore, the minimum yaw energy is achieved with a neither too large nor too small travel time.

These two tradeoffs imply that we have to balance the energy components for surge, heave, and yaw controls with an optimal travel time to minimize the total energy used.

V. Simulation Results and Analysis

In this section, we validate the effectiveness of the proposed approach in two steps with different current conditions. First, the proposed approach is evaluated with the same scenario in Section III and compared with the DC solution. Secondly, extensive simulations are performed to compare the proposed approach with a LOS-based control scheme for AUVs on a more realistic mission profile. Finally, discussions are made in terms of the tuning parameters and possible extensions of the proposed EMPC.

TABLE I
ENERGY CONSUMPTION COMPARISON BETWEEN THE DC AND EO-EMPC

Flow condition	DC	EO-EMPC	Loss
#1	177.45 J	179.31 J	1.05%
#2	411.03 J	416.08 J	1.23%
#3	392.53 J	393.24 J	0.18%
#4	211.30 J	212.47 J	0.56%

A. Comparison With the DC

To validate that the EMPC based on approximated energy-to-go leads to performance close to the DC solution, we apply the proposed approach to the same mission profile in Section III. We select the following four conditions with constant ocean current velocity to make the problem computationally manageable for the DC.

1) $U_c = 0$ m/s and $\psi_c = 0°$.
2) $U_c = 0.160$ m/s and $\psi_c = -66.21°$.
3) $U_c = 0.105$ m/s and $\psi_c = -135.41°$.
4) $U_c = 0.054$ m/s and $\psi_c = 141.92°$.

Here, $U_c = ((V_c^x)^2 + (V_c^y)^2)^{1/2}$ and $\psi_c = \text{atan2}(V_c^y, V_c^x)$ are the magnitude and direction of the ocean currents, respectively. For EMPC, the time step sizes within the prediction horizon and the prediction horizon are 0.1 and 1 s, respectively. We choose $\beta = 1$. The optimization in EMPC is solved with fmincon in MATLAB. The simulation of the vehicle motion is performed in MATLAB with the six-DOF model presented in Section II-A. The energy consumption from the EO-EMPC and DC is summarized in Table I, and the vehicle trajectories are given in Fig. 11. It can be observed that both controllers drive the vehicle to visit all the waypoints with a satisfactory vehicle pose, and EO-EMPC can achieve near-optimal energy efficiency under different flow conditions. Meanwhile, it is noteworthy that a significant reduction in computation time is achieved by EO-EMPC (i.e., the average CPU time for EO-EMPC is about 0.1 s) by using approximated energy-to-go. The comparison of the vehicle relative velocities from both approaches for the flow condition #1 is also provided in Fig. 12. From Fig. 12, we see that EO-EMPC mimics the DC solution, e.g., it reduces the relative surge velocity during turning to save energy.

B. Comparison With a LOS-Based Approach

To further demonstrate the effectiveness of EO-EMPC, we consider a lawnmower-type mission where the x and y locations of the waypoints are $\text{WP}_i \in \{(0,0), (50,0), (50,10), (0,10), (0,20), (50,20), (50,30), (0,30), (0,40), (50,40), (50,50), (0,50), (0,0)\}$ m. This lawnmower path represents a mission where the vehicle surveys or maps an area (e.g., [30], [31]). Five different current conditions are selected for performance comparison. The current condition #5 has zero current velocity over the entire operating domain. The current conditions #6–#9 are selected among the ocean current data obtained from U.S. Integrated Ocean Observing System High Frequency Radar Network (HFRNet) [32]. The flow data for the region near Long Island in New York from March 24, 2019, to March 25, 2019, are linearly interpolated

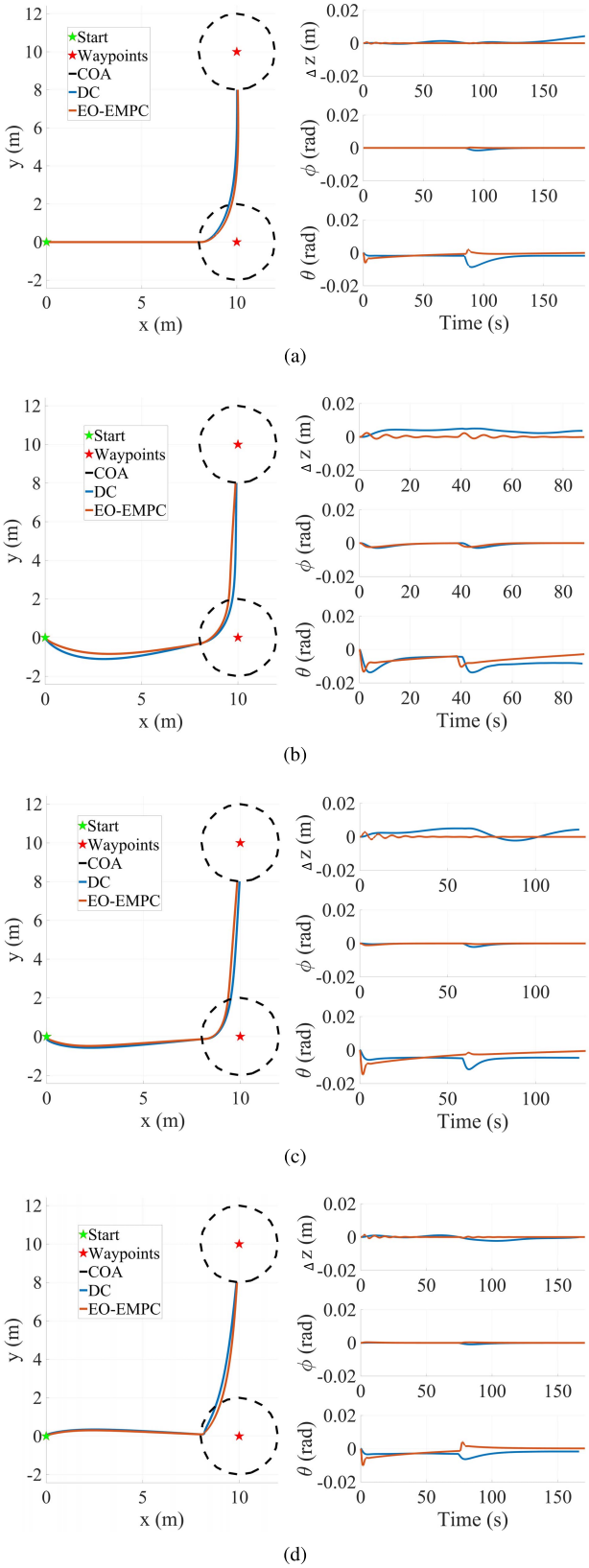

Fig. 11. Vehicle trajectories from the DC and EO-EMPC under different flow conditions (Δz denotes the deviation from the desired depth). (a) Flow condition #1. (b) Flow condition #2. (c) Flow condition #3. (d) Flow condition #4.

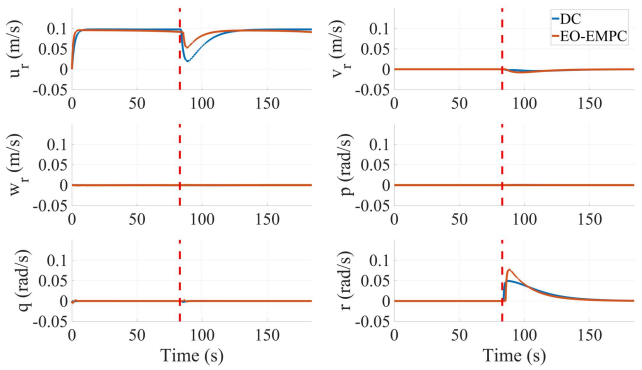

Fig. 12. Vehicle relative velocities from the DC and EO-EMPC under flow condition #1 (red dashed line indicates the instance when the vehicle switches its destination to the second waypoint).

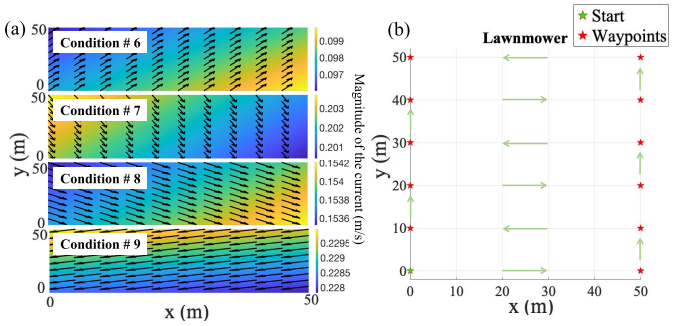

Fig. 13. Setup of the mission. (a) Current conditions. (b) Mission profile; green arrows indicate the sequence of the waypoints.

between spatial and temporal grid points to simulate the flow field. The patterns of the chosen current conditions and the setup of the waypoints are given in Fig. 13.

Since solving the above mission profiles using the DC is computationally prohibitive, the LOS guidance-based approach is adopted for comparison as it represents a conventional solution for the mission. In particular, the energy-optimal LOS-based approach of [33] is implemented, which uses an MPC to control the horizontal thrusters for tracking an energy-optimal surge speed setpoint and a yaw angle setpoint from the LOS guidance. Two individual PID controllers are employed for the vertical thruster control to maintain zero pitch angle and a constant depth. The yaw angle setpoint is computed as [34]

$$\psi_s = \gamma_d - \tan^{-1}\left(\frac{v_r + v_c}{u_r + u_c}\right) \tag{23}$$

where $\gamma_d = \gamma_c - \tan^{-1}(y_e/d_{\text{los}})$ represents the desired course direction of the vehicle, γ_c is the course direction between the present and past waypoints, y_e is the distance from the vehicle location to the line linking the present and past waypoints (i.e., cross-track error), and d_{los} is the lookahead distance. The second term on the right of (23) compensates for the drift effect from currents. See Fig. 14 for an illustration of the LOS geometry. The lookahead distance is chosen as 2 m in this study. The setpoint for the relative surge velocity is computed by minimizing the energy for surge and heave controls within

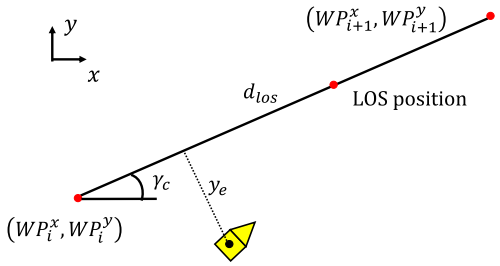

Fig. 14. Illustration of the LOS geometry.

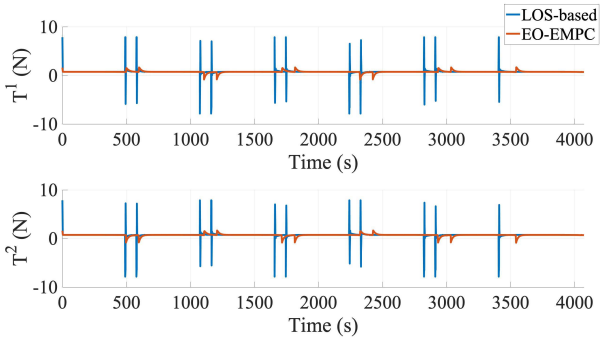

Fig. 15. Thrusts from the LOS-based approach and EO-EMPC under no current (i.e., flow condition #5).

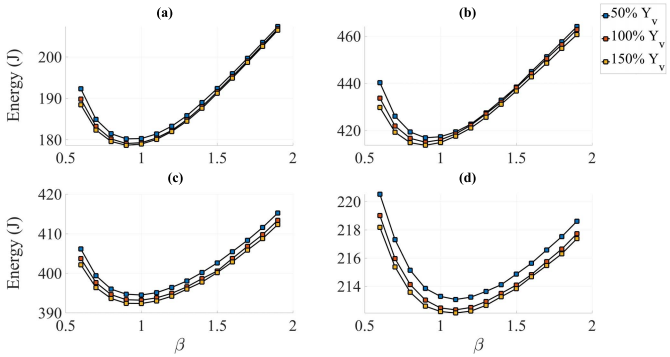

Fig. 16. Effect of β on the performance of EO-EMPC under different flow conditions and with different sway damping coefficients. (a) Flow condition #1. (b) Flow condition #2. (c) Flow condition #3. (d) Flow condition #4.

unit travel distance given as

$$u_s = \arg\min_{u_r} \frac{P^{\text{SD}} + P^{\text{PB}}}{U_{\text{rd}}} \tag{24}$$

where U_{rd} is the vehicle speed projected onto γ_d expressed as

$$U_{\text{rd}} = \sqrt{u_r^2 + v_r^2 - (U_c \sin\psi_{\text{cd}})^2} + U_c \cos\psi_{\text{cd}} \tag{25}$$

and $\psi_{\text{cd}} = \psi_c - \gamma_d$. The optimization in (24) is subject to the constraint that the vehicle relative surge velocity must be large enough to permit a positive U_{rd}.

Based on the above setup, we simulate the EO-EMPC and the LOS-based approach, and summarize the vehicle performance in Table II. The average cross-track error is computed by averaging vehicle deviations from the line between the present and past waypoints when the vehicle is outside the COA. From Table II, it is verified that EO-EMPC can

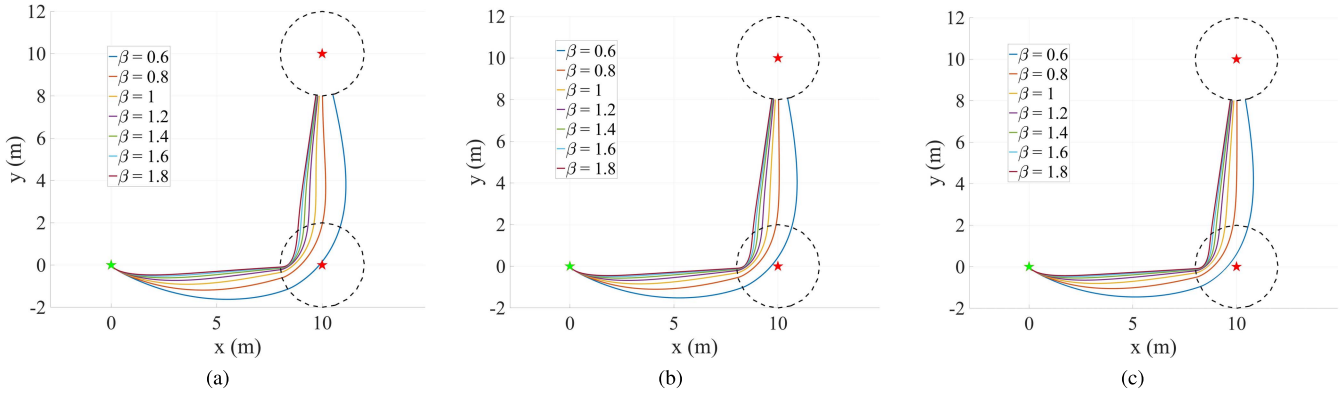

Fig. 17. Vehicle trajectories of EO-EMPC with different choices of β under flow condition #2. (a) $Y_v = 5$ kg/s (50% of the nominal). (b) $Y_v = 10$ kg/s (nominal). (c) $Y_v = 15$ kg/s (150% of the nominal).

TABLE II
PERFORMANCE COMPARISON BETWEEN THE LOS-BASED APPROACH AND EO-EMPC

Flow condition	Energy Consumption			Travel time			Average cross-track error	
	LOS-based	EO-EMPC	Reduction	LOS-based	EO-EMPC	Increase	LOS-based	EO-EMPC
#5	5459.9 J	3906.5 J	39.76%	3922.8 s	4061.4 s	3.53%	0.035 m	0.044 m
#6	6834.0 J	5210.5 J	31.16%	3040.2 s	3097.1 s	1.87%	0.043 m	0.288 m
#7	9785.3 J	8852.6 J	10.54%	1684.5 s	1760.6 s	4.52%	0.045 m	0.579 m
#8	8707.6 J	7728.5 J	12.67%	1905.0 s	1969.0 s	3.36%	0.043 m	0.571 m
#9	10547.1 J	9480.5 J	11.25%	1604.3 s	1687.7 s	5.20%	0.039 m	0.568 m

significantly reduce the vehicle control energy when following the waypoints. To further illustrate the advantage of EO-EMPC, the horizontal thrusts from the LOS-based approach and EO-EMPC under the current condition #5 are compared in Fig. 15. It can be seen that EO-EMPC reduces the energy consumption by avoiding the spikes in the thruster inputs during the vehicle turning. On the downside, the EO-EMPC has a slightly longer traveling time and larger average cross-track error than that from the LOS-based approach across all cases as the EO-EMPC only aims at minimizing the vehicle energy consumption.

C. Discussions

Discussions are made in the following aspects concerning the use of the proposed approach in real-world applications.

1) Choice of the Parameter β: When formulating the EMPC, β is introduced as a tuning parameter to characterize the relationship between the required heading variation in the dynamic mode (ψ_d) and the difference between the desired and present course directions of the vehicle at the end of the prediction horizon ($\Delta\psi_{H|t}$). As shown in Fig. 8, the vehicle has to change its heading by at least $\Delta\psi_{H|t}$ to head toward the destination. In reality, since the vehicle will be moving forward and subject to induced sway motion while turning, ψ_d must be larger than $\Delta\psi_{H|t}$ to compensate for the drift during the turning, i.e., $\beta > 0.5$. Meanwhile, the performance of the control will be affected by the choice of β. In particular, a too large or too small β will lead to a sharp or a slow turn, respectively, resulting in deteriorated energy efficiency.

To illustrate the effect of β on the control performance, the energy consumed by EO-EMPC with different β's on the mission profile in Section V-A under different flow conditions and sway damping coefficient values is compared in Fig. 16. The vehicle trajectories of EO-EMPC with different β's under flow condition #2 are also provided in Fig. 17. Figs. 16 and 17 show that a constant value of $\beta \approx 1$ yields near-optimal vehicle energy efficiency under different conditions, suggesting that it may be used for different real-world applications.

2) Regulation of the Cross-Track Error: In this work, we investigate the waypoint tracking problem, and the proposed EO-EMPC takes no consideration of the cross-track error. However, the proposed approach can be modified to address the path following problem by including a term related to the cross-track error in the terminal cost of EMPC as follows:

$$E = P_d\Gamma_d + P_s\Gamma_s + w_{\text{ct}}y_{e,H|t}^2 \tag{26}$$

where w_{ct} is a constant factor penalizing a large cross-track error and $y_{e,H|t}$ is the cross-track error of the vehicle state at the end of the prediction horizon. Since the vehicle will be performing the waypoint transition inside the COA, the cross-track error is not considered (i.e., $y_{e,H|t} = 0$) when the vehicle is in the COA. The performance of the EO-EMPC using the terminal cost in (26) with different choices of w_{ct} on the mission profile in Section V-A under flow condition #2 is summarized in Fig. 18. It can be seen that a smaller average cross-track error can be achieved with a larger w_{ct} in the modified terminal cost. Meanwhile, energy efficiency will be compromised for a larger w_{ct} as the vehicle may need to

turn drastically to reduce the cross-track error. In real-world applications, the value of w_{ct} can be determined by the user to satisfy different mission requirements and reflect the proper tradeoff between energy efficiency and path following.

VI. Conclusion

In this article, we investigate the energy-optimal control problem of AUVs under ocean currents. To develop an optimal control strategy feasible for onboard applications, an EO-EMPC that uses EMPC for horizontal thruster control and PIDs for vertical thruster control is proposed. In order to obtain energy efficiency close to that of the DC, the terminal cost in EMPC is formulated as the approximated energy-to-go. Based on the characteristics of the optimal maneuver in the DC solution, we partition the energy-to-go into dynamic and static parts, and parameterize them based on their durations, the destination, vehicle dynamics, and ocean currents. Extensive analysis of the approximated energy-to-go shows that it captures the tradeoffs among different energy-consuming components for surge, heave, and yaw controls. Simulation evaluation is first conducted by comparing EO-EMPC with the DC and demonstrates that EO-EMPC can achieve near-optimal energy efficiency. Further simulation analysis is performed on a lawnmower path under different current conditions. By comparing EO-EMPC with the LOS-based approach, it is demonstrated that EO-EMPC can achieve substantial energy reductions by leveraging the vehicle dynamics and current information.

Future work will focus on the experimental validation of the proposed approach on the test-bed AUV, DROP-Sphere. In this

$$
\begin{aligned}
P_d &= P^{\text{PB}} + \sum_{i=1}^{2} \frac{h_p\left(T^i_{H|t}\right) + 2h_p\left(T^i_{H+1|t}\right) + h_p\left(T^i_{H+2|t}\right)}{4} \\
&\text{Substituting (15) and (16):} \\
&= P^{\text{PB}} + \frac{\alpha}{4}\Bigg(\left(\frac{X_u u_{r,H|t}}{2} + \frac{m_r a_1 + N_r r_{H|t}}{2l_2}\right)^2 + \left(\frac{X_u u_{r,H|t}}{2} - \frac{m_r a_1 + N_r r_{H|t}}{2l_2}\right)^2 \\
&\qquad + \left(\frac{X_u u_{r,H|t}}{2} + \frac{m_r a_1 + N_r r_{\max}}{2l_2}\right)^2 + \left(\frac{X_u u_{r,H|t}}{2} - \frac{m_r a_1 + N_r r_{\max}}{2l_2}\right)^2 + \left(\frac{X_u u_{r,H|t}}{2} + \frac{m_r a_2 + N_r r_{\max}}{2l_2}\right)^2 \\
&\qquad + \left(\frac{X_u u_{r,H|t}}{2} - \frac{m_r a_2 + N_r r_{\max}}{2l_2}\right)^2 + \left(\frac{X_u u_{r,H|t}}{2} + \frac{m_r a_2}{2l_2}\right)^2 + \left(\frac{X_u u_{r,H|t}}{2} - \frac{m_r a_2}{2l_2}\right)^2\Bigg) \\
&= P^{\text{PB}} + 2\alpha\left(\frac{X_u u_{r,H|t}}{2}\right)^2 + \frac{\alpha}{2}\Bigg(\left(\frac{m_r a_1 + N_r r_{H|t}}{2l_2}\right)^2 + \left(\frac{m_r a_1 + N_r r_{\max}}{2l_2}\right)^2 + \left(\frac{m_r a_2 + N_r r_{\max}}{2l_2}\right)^2 + \left(\frac{m_r a_2}{2l_2}\right)^2\Bigg) \\
&= P^{\text{PB}} + P^{\text{SD}} + \frac{\alpha}{8l_2^2}\big(m_r^2 a_1^2 + 2m_r a_1 N_r r_{H|t} + N_r^2 r_{H|t}^2 + m_r^2 a_1^2 + 2m_r a_1 N_r r_{\max} + N_r^2 r_{\max}^2 + m_r^2 a_2^2 \\
&\qquad + 2m_r a_2 N_r r_{\max} + N_r^2 r_{\max}^2 + m_r^2 a_2^2\big) \\
&= P^{\text{PB}} + P^{\text{SD}} + \frac{\alpha}{8l_2^2}\big(2m_r^2 a_1^2 + 2m_r a_1 N_r r_{H|t} + N_r^2 r_{H|t}^2 + 2m_r N_r r_{\max}(a_1 + a_2) + 2N_r^2 r_{\max}^2 + 2m_r^2 a_2^2\big) \\
&\text{Substituting } a_1 = 2\frac{r_{\max} - r_{H|t}}{\Gamma_d},\ a_2 = -2\frac{r_{\max}}{\Gamma_d}, \text{ and } r_{\max} = 2\frac{\psi_d}{\Gamma_d} - \frac{r_{H|t}}{2}: \\
&= P^{\text{PB}} + P^{\text{SD}} + \frac{\alpha}{8l_2^2}\Bigg(N_r^2 r_{H|t}^2 + \frac{8m_r^2 r_{H|t}^2}{\Gamma_d^2} - \frac{4m_r N_r r_{H|t}^2}{\Gamma_d} + \left(\frac{16m_r^2}{\Gamma_d^2} + 2N_r^2\right)\left(\frac{4\psi_d^2}{\Gamma_d^2} - \frac{2\psi_d r_{H|t}}{\Gamma_d} + \frac{r_{H|t}^2}{4}\right) \\
&\qquad - \frac{16m_r^2 r_{H|t}}{\Gamma_d^2}\left(2\frac{\psi_d}{\Gamma_d} - \frac{r_{H|t}}{2}\right)\Bigg) \\
&= P^{\text{PB}} + P^{\text{SD}} + c_0 + \frac{c_1}{\Gamma_d} + \frac{c_2}{\Gamma_d^2} + \frac{c_3}{\Gamma_d^3} + \frac{c_4}{\Gamma_d^4} \\
&= P^{\text{PB}} + P^{\text{SD}} + P^{\text{yaw}}
\end{aligned}
\tag{27}
$$

where

$$
c_0 = \frac{3\alpha r_{H|t}^2 N_r^2}{16l_2^2}, \quad c_1 = -\frac{\alpha\left(m_r N_r r_{H|t}^2 + N_r^2 \psi_d r_{H|t}\right)}{2l_2^2}, \quad c_2 = \frac{\alpha\left(5m_r^2 r_{H|t}^2 + 2N_r^2 \psi_d^2\right)}{2l_2^2} \tag{28a}
$$

$$
c_3 = -\frac{\alpha\left(8m_r^2 r_{H|t}\psi_d\right)}{l_2^2}, \quad c_4 = \frac{8m_r^2 \psi_d^2}{l_2^2} \tag{28b}
$$

and $m_r = I_{zz} - N_{\dot{r}}$.

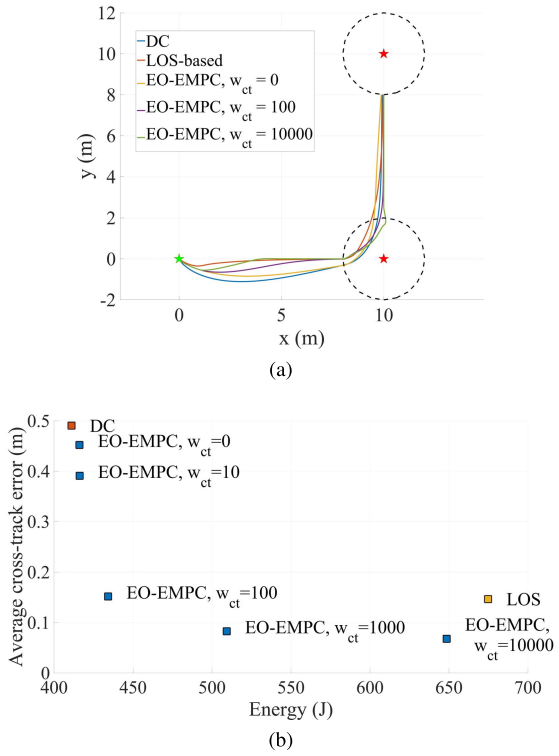

Fig. 18. Performance of the EO-EMPC modified for path following with different choices of w_{ct} under flow condition #2. (a) Vehicle trajectory. (b) Energy and average cross-track error comparison.

work, it is assumed that the knowledge of the vehicle states and ocean currents is perfect, which can be difficult to achieve on some low-cost AUV platforms. Therefore, in the future, we will investigate the robustness of the proposed approach under uncertainty in the state estimation and ocean current prediction. Finally, for typical AUVs, the vehicle hydrodynamic coefficients can vary depending on the vehicle payloads and environmental conditions. Thus, validating the vehicle models used in this study and investigating the adaptation of the proposed control to handle the model mismatch will also be our future focus.

APPENDIX I
DROP-SPHERE MODEL PARAMETERS

$$m = 20.42 \text{ kg} \quad I_{xx} = 0.1205 \text{ kg} \cdot \text{m}^2$$
$$x_g = 0 \text{ m} \quad y_g = 0 \text{ m}$$
$$l_1 = 0.2794 \text{ m} \quad l_2 = 0.1694 \text{ m}$$
$$Y_{\dot{v}} = -20 \text{ kg} \quad Z_{\dot{w}} = -40 \text{ kg}$$
$$N_{\dot{r}} = -2 \text{ kg} \cdot \text{m}^2/\text{rad} \quad X_u = 15 \text{ kg/s}$$
$$K_p = 10 \text{ kg} \cdot \text{m}^2/(\text{s} \cdot \text{rad}) \quad M_q = 5 \text{ kg} \cdot \text{m}^2/(\text{s} \cdot \text{rad})$$
$$I_{yy} = 0.9431 \text{ kg} \cdot \text{m}^2 \quad I_{zz} = 1.0061 \text{ kg} \cdot \text{m}^2$$
$$z_g = 0.00178 \text{ m} \quad z_b = -0.009 \text{ m}$$
$$l_3 = -0.0204 \text{ m} \quad X_{\dot{u}} = -10 \text{ kg}$$
$$K_{\dot{p}} = -2 \text{ kg} \cdot \text{m}^2/\text{rad} \quad M_{\dot{q}} = -2 \text{ kg} \cdot \text{m}^2/\text{rad}$$
$$Y_v = 10 \text{ kg/s} \quad Z_w = 10 \text{ kg/s}$$
$$N_r = 5 \text{ kg} \cdot \text{m}^2/(\text{s} \cdot \text{rad}).$$

APPENDIX II
DERIVATION OF THE APPROXIMATED POWER IN THE DYNAMIC MODE

(27), (28a), and (28b), as shown at the bottom of the previous page.

ACKNOWLEDGMENT

The authors would like to thank Dr. C. Barbalata of Louisiana State University, and Dr. E. I. Rüland for providing details of the AUV model during the course of this article.

REFERENCES

[1] J.-S. Wang and C. S. G. Lee, "Self-adaptive recurrent neuro-fuzzy control of an autonomous underwater vehicle," *IEEE Trans. Robot. Autom.*, vol. 19, no. 2, pp. 283–295, Apr. 2003.
[2] K. Zwolak and A. Felski, "Current state of deep ocean bathymetric exploration," *Annu. Navigat.*, vol. 24, no. 1, pp. 257–267, Dec. 2017.
[3] D. Chang, F. Zhang, and C. R. Edwards, "Real-time guidance of underwater gliders assisted by predictive ocean models," *J. Atmos. Ocean. Technol.*, vol. 32, no. 3, pp. 562–578, 2015.
[4] S. Williams *et al.*, "Monitoring of benthic reference sites: Using an autonomous underwater vehicle," *IEEE Robot. Autom. Mag.*, vol. 19, no. 1, pp. 73–84, Mar. 2012.
[5] D. Kruger, R. Stolkin, A. Blum, and J. Briganti, "Optimal AUV path planning for extended missions in complex, fast-flowing estuarine environments," in *Proc. IEEE Int. Conf. Robot. Autom.*, Apr. 2007, pp. 4265–4270.
[6] J. Witt and M. Dunbabin, "Go with the flow: Optimal AUV path planning in coastal environments," in *Proc. Austral. Conf. Robot. Autom.*, 2008, pp. 1–9.
[7] A. Alvarez, A. Caiti, and R. Onken, "Evolutionary path planning for autonomous underwater vehicles in a variable ocean," *IEEE J. Ocean. Eng.*, vol. 29, no. 2, pp. 418–429, Apr. 2004.
[8] D. N. Subramani, T. Lolla, P. J. Haley, and P. F. Lermusiaux, "A stochastic optimization method for energy-based path planning," in *Proc. Int. Conf. Dyn. Data-Driven Environ. Syst. Sci.*, 2014, pp. 347–358.
[9] P. Raja and S. Pugazhenthi, "Optimal path planning of mobile robots: A review," *Int. J. Phys. Sci.*, vol. 7, no. 9, pp. 1314–1320, Feb. 2012.
[10] C. Shen, Y. Shi, and B. Buckham, "Integrated path planning and tracking control of an AUV: A unified receding horizon optimization approach," *IEEE/ASME Trans. Mechatronics*, vol. 22, no. 3, pp. 1163–1173, Jun. 2017.
[11] S. Heshmati-Alamdari, G. C. Karras, P. Marantos, and K. J. Kyriakopoulos, "A robust predictive control approach for underwater robotic vehicles," *IEEE Trans. Control Syst. Technol.*, vol. 28, no. 6, pp. 2352–2363, Nov. 2020.
[12] B. Claus and R. Bachmayer, "Energy optimal depth control for long range underwater vehicles with applications to a hybrid underwater glider," *Auto. Robots*, vol. 40, no. 7, pp. 1307–1320, Oct. 2016.
[13] N. Wang, Y. Gao, and X. Zhang, "Data-driven performance-prescribed reinforcement learning control of an unmanned surface vehicle," *IEEE Trans. Neural Netw. Learn. Syst.*, vol. 32, no. 12, pp. 5456–5467, Dec. 2021.
[14] N. Wang, Y. Gao, H. Zhao, and C. K. Ahn, "Reinforcement learning-based optimal tracking control of an unknown unmanned surface vehicle," *IEEE Trans. Neural Netw. Learn. Syst.*, vol. 32, no. 7, pp. 3034–3045, Jul. 2021.
[15] E. Bohn, E. M. Coates, S. Moe, and T. A. Johansen, "Deep reinforcement learning attitude control of fixed-wing UAVs using proximal policy optimization," in *Proc. Int. Conf. Unmanned Aircr. Syst. (ICUAS)*, Jun. 2019, pp. 523–533.
[16] N. Yang, M. R. Amini, M. Johnson-Roberson, and J. Sun, "Real-time model predictive control for energy management in autonomous underwater vehicle," in *Proc. IEEE Conf. Decis. Control (CDC)*, Dec. 2018, pp. 4321–4326.
[17] N. Yang, D. Chang, M. R. Amini, M. Johnson-Robersor, and J. Sun, "Energy management for autonomous underwater vehicles using economic model predictive control," in *Proc. Amer. Control Conf. (ACC)*, Jul. 2019, pp. 2639–2644.

[18] E. Iscar, C. Barbalata, N. Goumas, and M. Johnson-Roberson, "Towards low cost, deep water AUV optical mapping," in *Proc. OCEANS*, Oct. 2018, pp. 1–6.
[19] L. Lapierre, "Robust diving control of an AUV," *Ocean Eng.*, vol. 36, no. 1, pp. 92–104, 2009.
[20] W. Caharija *et al.*, "Integral line-of-sight guidance and control of underactuated marine vehicles: Theory, simulations, and experiments," *IEEE Trans. Control Syst. Technol.*, vol. 24, no. 5, pp. 1623–1642, Sep. 2016.
[21] A. M. Lekkas and T. I. Fossen, "Line-of-sight guidance for path following of marine vehicles," in *Advanced in Marine Robotics*, O. Gal, Ed. San Francisco, CA, USA: Academic, 2013, ch. 5, pp. 63–92.
[22] T.-H. Joung, K. Sammut, F. He, and S.-K. Lee, "Shape optimization of an autonomous underwater vehicle with a ducted propeller using computational fluid dynamics analysis," *Int. J. Nav. Archit. Ocean Eng.*, vol. 4, no. 1, pp. 44–56, Mar. 2012.
[23] B. Garau, A. Alvarez, and G. Oliver, "AUV navigation through turbulent ocean environments supported by onboard H-ADCP," in *Proc. IEEE Int. Conf. Robot. Autom.*, May 2006, pp. 3556–3561.
[24] O. Hegrenæs and Ø. Hallingstad, "Model-aided INS with sea current estimation for robust underwater navigation," *IEEE J. Ocean. Eng.*, vol. 36, no. 2, pp. 316–337, Apr. 2011.
[25] L. Medagoda, S. B. Williams, O. Pizarro, J. C. Kinsey, and M. V. Jakuba, "Mid-water current aided localization for autonomous underwater vehicles," *Auton. Robots*, vol. 40, no. 7, pp. 1207–1227, Oct. 2016.
[26] O. Stryk, "Numerical solution of optimal control problems by direct collocation," in *Optimal Control: Calculus of Variations, Optimal Control Theory and Numerical Methods*, vol. 129. Basel, Germany: Birkhaüser, 1993.
[27] C.-K. Ryoo, H.-S. Shin, and M.-J. Tahk, "Energy optimal waypoint guidance synthesis for antiship missiles," *IEEE Trans. Aerosp. Electron. Syst.*, vol. 46, no. 1, pp. 80–95, Jan. 2010.
[28] J. B. Rawlings, D. Angeli, and C. N. Bates, "Fundamentals of economic model predictive control," in *Proc. IEEE 51st IEEE Conf. Decis. Control (CDC)*, Dec. 2012, pp. 3851–3861.
[29] T. G. McGee and J. K. Hedrick, "Optimal path planning with a kinematic airplane model," *J. Guid., Control, Dyn.*, vol. 30, no. 2, pp. 629–633, Mar. 2007.
[30] D. W. Caress *et al.*, "High-resolution multibeam, sidescan, and subbottom surveys using the MBARI AUV D. Allan B.," in *Marine Habitat Mapping Technology for Alaska*. Fairbanks, AK, USA: Alaska Sea Grant College Program, Univ. Alaska Fairbanks, 2008, pp. 47–69.
[31] S. B. Williams *et al.*, "Autonomous underwater vehicle-assisted surveying of drowned reefs on the shelf edge of the Great Barrier Reef, Australia," *J. Field Robot.*, vol. 27, no. 5, pp. 675–697, Sep. 2010.
[32] D. Barrick, V. Fernandez, M. I. Ferrer, C. Whelan, and Ø. Breivik, "A short-term predictive system for surface currents from a rapidly deployed coastal HF radar network," *Ocean Dyn.*, vol. 62, no. 5, pp. 725–740, May 2012.
[33] N. Yang, D. Chang, M. Johnson-Roberson, and J. Sun, "Robust energy-optimal path following control for autonomous underwater vehicles in ocean currents," in *Proc. Amer. Control Conf. (ACC)*, Jul. 2020, pp. 5119–5124.
[34] S. Moe and K. Y. Pettersen, "Set-based line-of-sight (LOS) path following with collision avoidance for underactuated unmanned surface vessels under the influence of ocean currents," in *Proc. IEEE Conf. Control Technol. Appl. (CCTA)*, Aug. 2017, pp. 241–248.

Niankai Yang (Graduate Student Member, IEEE) received the B.S. degree in naval architecture and ocean engineering from Shanghai Jiao Tong University, Shanghai, China, in 2016. He is currently pursuing the Ph.D. degree in naval architecture and marine engineering with the University of Michigan, Ann Arbor, MI, USA.

His current research interests include machine learning for condition monitoring of lithium-ion batteries, model predictive control and its application, and planning and control of autonomous vehicles.

Dongsik Chang (Member, IEEE) received the B.S. degree from Hanyang University, Seoul, South Korea, in 2007, and the M.S. and Ph.D. degrees from the Georgia Institute of Technology, Atlanta, GA, USA, in 2010 and 2016, respectively, all in electrical and computer engineering.

He spent about two years in the industry, working with Samsung Electronics, Seoul, as a Senior Engineer. He held a Research Fellow position with the University of Michigan, Ann Arbor, MI, USA. He is currently a Post-Doctoral Scholar with Oregon State University, Corvallis, OR, USA. His research lies at the intersection of systems and control, and robotics. His research interests include marine robotics, active perception, intelligent autonomous systems, control theory, mobile sensor networks, multiagent systems, and machine learning.

Matthew Johnson-Roberson received the B.S. degree from Carnegie Mellon University, Pittsburgh, PA, USA, and the Ph.D. degree from the University of Sydney, Sydney, NSW, Australia, in 2010.

He has held post-doctoral positions with the KTH Royal Institute of Technology, Stockholm, Sweden, and the Australian Center for Field Robotics, Sydney, Australia. He was a Faculty with the University of Michigan, Ann Arbor, USA. He is currently a Professor in the Robotics Institute in the School of Computer Science at Carnegie Mellon University. His current research interests include the processing and interpretation of three-dimensional data, specifically 3-D reconstruction, segmentation, machine learning, and robotic vision.

Dr. Johnson-Roberson was a recipient of the NSF CAREER Award in 2015.

Jing Sun (Fellow, IEEE) received the Ph.D. degree from the University of Southern California, Los Angeles, CA, USA, in 1989.

She is currently the Michael G. Parsons Collegiate Professor with the Department of Naval Architecture and Marine Engineering, with joint appointments with the Department of Electrical Engineering and Computer Science, and the Department of Mechanical Engineering, University of Michigan, Ann Arbor, MI, USA. Her research interests include modeling, control, and optimization of dynamic systems, with applications to marine and automotive systems.

Dr. Sun is a fellow of the National Academy of Inventors, the International Federation of Automatic Control (IFAC), and the Society of Naval Architects and Marine Engineers. She was a recipient of the 2003 IEEE Control System Technology Award.